





Photonic Devices with Multi-Domain Liquid Crystal Structures

Aleksey Kudreyko ^{1,*} , Vladimir Chigrinov ^{2,3,4} , Kristiaan Neyts ² , Denis Chausov ^{5,6} 
and Arina Perestoronina ¹

¹ Department of General Physics, Ufa University of Science and Technology, 450076 Ufa, Russia; arina.perest@yandex.ru

² Department of Electronic and Computer Engineering, Hong Kong University of Science and Technology, Clear Water Bay, Kowloon 999077, Hong Kong; eechigr@ust.hk (V.C.); eeneyts@ust.hk (K.N.)

³ Nanjing Jingcui Optical Technology Co., Ltd., Nanjing 211135, China

⁴ Department of Fundamental Physics and Nanotechnology, State University of Education, 105005 Moscow, Russia

⁵ Prokhorov General Physics Institute of the Russian Academy of Sciences, 119991 Moscow, Russia; d.chausov@yandex.ru

⁶ Department of Digital Economy, Moscow University for Industry and Finance “Synergy”, 105318 Moscow, Russia

* Correspondence: akudreyko@uust.ru

Abstract: Photoalignment by azo dye nanolayers can provide high alignment quality for large-area liquid crystal devices. Application of this technology to active optical elements for signal processing and communications is a hot topic of photonics research. In this article, we review recent demonstrations and performance of liquid crystal photonic devices, discuss the advantages of the proposed technology, and identify challenges and future prospects in the research field of photoaligned multi-domain liquid crystal structures. We believe that the developments discussed here can provide directions for future research and potential opportunities for applications of liquid crystal devices based on multi-domain photoalignment.

Keywords: liquid crystals; photoalignment; LC sensors; field sequential color display; security films; phase modulation; liquid crystal lens



Citation: Kudreyko, A.; Chigrinov, V.; Neyts, K.; Chausov, D.; Perestoronina, A. Photonic Devices with Multi-Domain Liquid Crystal Structures. *Crystals* **2024**, *14*, 512. <https://doi.org/10.3390/cryst14060512>

Academic Editor: Francesco Simoni

Received: 30 April 2024

Revised: 7 May 2024

Accepted: 27 May 2024

Published: 28 May 2024



Copyright: © 2024 by the authors. Licensee MDPI, Basel, Switzerland. This article is an open access article distributed under the terms and conditions of the Creative Commons Attribution (CC BY) license (<https://creativecommons.org/licenses/by/4.0/>).

1. Introduction

Over the past 25 years, advances in liquid crystal (LC) technology have given rise to the emergence of optical materials for the fabrication of advanced photonic devices [1]. This success was due to the synthesis of azo dyes that can form thin films with the functionality to provide predetermined surface alignment of LCs by using linearly polarized light [2]. As a result, it became possible to realize the potential of LC films as three-dimensionally structured anisotropic optical materials for the fabrication of thin-film optical devices based on spatial modulation of geometric phase. Nowadays, there exists a number of azo dye compounds for photoalignment of LC: brilliant yellow, sulfonic dye 1 (SD1), methyl red, etc. [3,4]. A variety of modifications and improvements were suggested three decades after the initial discovery [5]. A combination of multiple illumination steps through a photomask with homogeneous polarization provides patterned alignment of the surface [6]. The manipulation of multi-dimensional solitons on the photoaligned surface is beneficial for holography alignment [7]. Through these studies, it has been identified that photoaligned multi-domain LC structures are beneficial for photonic applications.

Commercial application of photoalignment technology is already applied in the ProMotion technology, which enables adaptive screen-refresh rates ranging from 24 to 120 Hz [8]. In addition to photoaligned LC displays, many other applications have been proposed and demonstrated (e.g., [9,10]). Applications of photoalignment in active optical elements for optical signal processing and communication are widespread in photonics research [11–13].

Simulation of various average LC orientations after exposure to linearly polarized light represents an emerging trend in terms of fundamental research [14].

This article shows relevant research in photoaligned azo dye nanolayers for a variety of applications and discusses the physics of the devices. The proposed technique of photoalignment does not involve any photochemical or structural transformations of the molecules [15]. New photoaligning films are robust and acceptable for applications with optically controlled anchoring energy. This is useful for photovoltaic, optoelectronic, and photonic devices. Such novel and highly ordered layer structures of organic molecules exhibit certain physical properties similar to aligned LC layers.

This article is organized as follows. In Section 2, we briefly review the physics of photoalignment technology. Then, we evaluate the physical mechanisms of beam transmittance through a security film, field sequential color displays, LC lenses, and sensors (Section 3). Finally, applications of photoaligned multi-domain LC devices are discussed in the conclusion.

2. Photoalignment Based on Azo Dye Nanolayers

Irradiation of azo dye molecules by linearly polarized light leads to light absorption in such a way that the potential energy of interaction between electromagnetic waves and azo dye nanolayer spontaneous polarization is proportional to $\cos^2\theta$, where θ is the angle between the absorption oscillator (parallel to the long axis of the azo dye molecules) and the polarization plane (see Figure 1a). As a result, azo dye molecules have an excess of energy and randomly reorient to minimize the potential energy. In other words, this is a process of the formation of equilibrium statistical distribution of potential energy over the rotational degrees of freedom of molecules, and it is described by the rotational diffusion model [16]. Typically, the exposure process lasts from 10 to 60 s and the exposure time depends on the azo dye thickness.

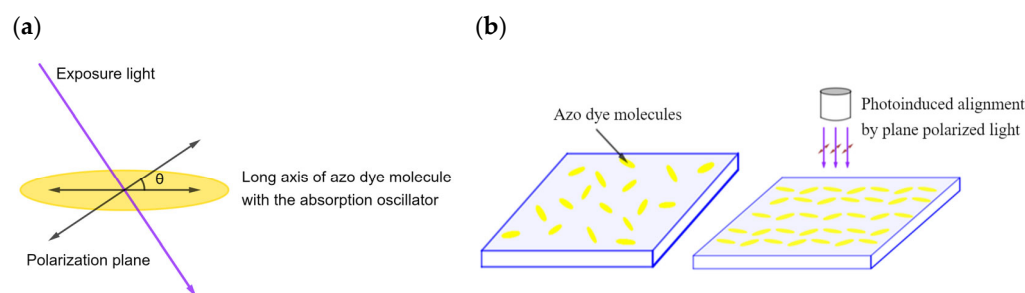


Figure 1. (a) Photoinduced ordering of photochemical stable azo dye films: (a) model of azo dye molecule and the absorption oscillator (azo-benzene -N=N- groups); (b) photoinduced reorientation process of azo dye.

The typical thickness of the photosensitive layer is in the range 1–15 nm, and this is enough for LC alignment in the bulk; however, anchoring energy significantly decreases in nanometer-size films. This effect can be understood by a proposition that a photosensitive coating with a thickness of 1–2 nm forms island-shaped formations and long-range orientational order keeps the director alignment on the azo dye-free surface. Once a continuous film is obtained, LC alignment can be achieved with the desirable anchoring properties, where LC molecules adhere due to steric and van der Waals interactions.

An important property of photoalignment is the saturated dependence of the azimuthal anchoring energy versus the exposure energy ($\lambda = 365$ nm or 450 nm) [15]. Thus, the pretilt angle of LCs becomes controllable and the quality of the photoaligned LC cell is comparable with the rubbing technology (see Figure 2).

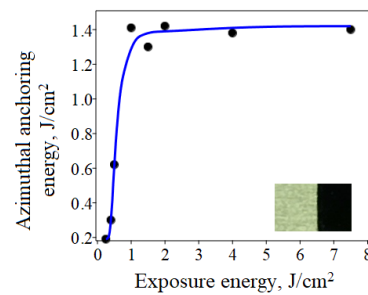


Figure 2. Continuous dependence of the azimuthal anchoring energy versus the exposure energy. Inset: observation of the alignment quality in the reflected light.

An important feature of this alignment method is the thermal and UV stability of azo dye nanolayers. This means that the impact of 100 °C during 24 h and UV illumination of 100 mW/cm² during 12 h does not have any effect on the electrooptic response of the LC cell. Another valuable feature of photoalignment is its applicability for curved plastic substrates, which do not tolerate high temperature, which is a problem for the imidization process in rubbing technology [17].

Below, we consider several applications of multi-domain photoalignment for various applications.

3. Applications of Photoalignment

Fabrication of patterned multi-domain photoaligned surface is possible by using two or more consecutive interference illumination steps [18]. This approach allows a variety of new patterns with submicrometer resolution to be fabricated [19]. It is expected that similar patterns can be useful for LC devices designed for diffractive optical gratings, light shutters, lenses, or beam steerers. Below we consider several applications of photoalignment.

3.1. Security Films

Authentication of encrypted information is required for applications in optical security [20]. As a result, there exists a growing interest in polarization control devices for multi-channel optical communication and advanced systems of optical security [21,22]. Previous research works suggest the fabrication of photocopy-protected devices and gadgets that are hard to counterfeit due to thin-film coatings with nanoscale encoding [23,24]. The working principle of first security films was based on chromaticity variation, a shift in reflectance spectra, etc. However, recent trends determine that verification of information must be carried out by means of non-contact photonic systems. Thus, passive imaging systems have become widely used in many devices against forgery and fraud [25].

In order to follow this trend, it has been suggested to manipulate the boundary conditions of LC layers, preferably realized through photoalignment. With this idea, patterned wave plates demonstrated the switching ability between predetermined images in the LC cell. Consequently, the anisotropy of LCs $\Delta n = n_{\parallel} - n_{\perp}$ induces relative phase retardation, which is defined as follows:

$$\Gamma = \frac{2\pi(n_{\parallel} - n_{\perp})d}{\lambda}, \quad (1)$$

where n_{\parallel} and n_{\perp} denote the refractive indices parallel and perpendicular to the in-plane slow axis, and λ is the wavelength of the irradiation light.

Modification of optically rewritable electronic paper represents a new class of highly counterfeit and simulation-resistant micro-optic security films that provide a wide range of visual effects for the public with different demands (supplementary video [26]). The required functionality of security films is provided by the multi-domain alignment of the LC film [27]. This works as follows: a photosensitive surface undergoes a number

of exposures by plane-polarized light through a photomask, and a patterned wave plate converts the polarized light to the desired polarization states (Figure 3).

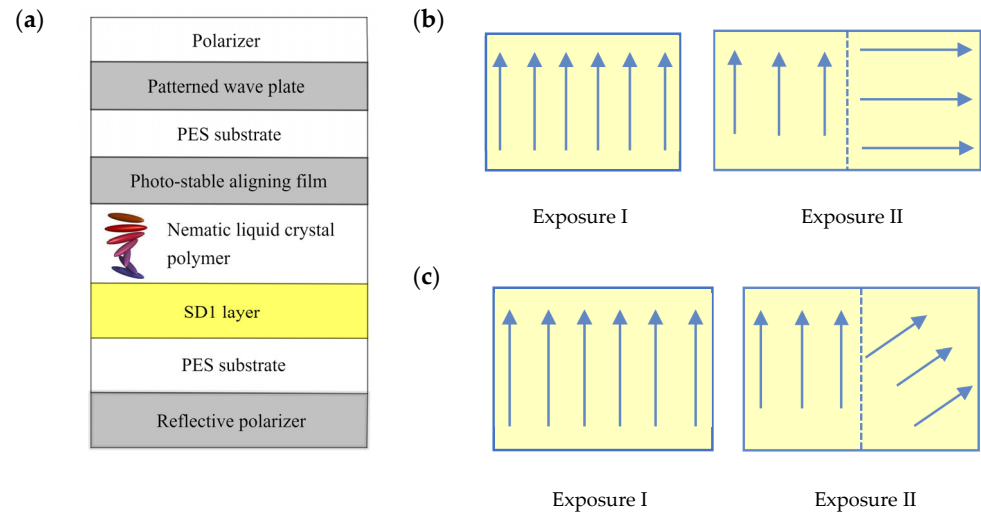


Figure 3. Color online: (a) Structure of experimental optical security film. Multi-step exposure for fabrication of patterned wave plate: (b) two-domain structure of quarter wave plate ($\Gamma = \pi/2$) and (c) half wave plate ($\Gamma = \pi$). Fast axes of the wave plates with different retardations are denoted by arrows.

Simulation of the reflected spectrum is achieved by splitting an LC layer into several sublayers with identical director configurations. This methodology enables each sublayer as a phase plate to be represented. The light intensity reflectance $R(\lambda)$ of the LC film sandwiched between polarizers can be obtained by using the Jones calculus. The spectral dependence $R(\lambda)$ is governed by the input polarizer angle α , half of the relative phase retardation $\delta = \Gamma/2$, and the twist angle Φ between the alignment directions of the substrates [28]. Here, the value of δ is explained by the case study, shown in Figure 4. Then, the reflectance at normal incidence is defined by the function $R = R(\alpha, \Phi, \delta)$ or

$$R = \left| \begin{pmatrix} \cos \alpha & \sin \alpha \\ \sin \alpha & -\cos \alpha \end{pmatrix} t_{LC}^T t_{LC} \begin{pmatrix} \cos \alpha \\ \sin \alpha \end{pmatrix} \right|^2,$$

where t_{LC} is the unimodular transmission Jones matrix of LC layer in the xy -plane under the assumption that light propagates along the z -axis, i.e., perpendicular to the surfaces (see Figure 3a). The fact that complex transmission functions are measured and radiation with well-defined polarization states is used means that unimodular transmission Jones matrix formalism can be used to analyze the spectrum:

$$t_{LC} = \begin{pmatrix} a + ib & -c + id \\ c + id & a - ib \end{pmatrix},$$

where the elements a, b, c , and d are defined by trigonometric relations

$$\begin{aligned} a &= \cos \chi \cos \Phi + \frac{\Phi}{\chi} \sin \chi \sin \Phi, & b &= \frac{\delta}{\chi} \sin \chi \cos \Phi; \\ c &= \cos \chi \sin \Phi - \frac{\Phi}{\chi} \sin \chi \cos \Phi, & d &= \frac{\delta}{\chi} \sin \chi \sin \Phi; \\ & & \chi &= \sqrt{\Phi^2 + \delta^2}. \end{aligned}$$

The starting point for the calculation of reflectance spectra is the so-called parameter space approach [29]. The reflectance of this security film is a unique function of the angle α , Φ , and δ and the thickness–birefringence product Δnd . For certain values of Δnd , the reflectance spectrum has a pronounced maximum. In other words, Δnd is the most

dominant parameter in the model. Color dispersion of Δnd enables colors in the security film to be produced. By fixing parameters α and Φ for a certain cell, it is possible to simulate the spectral dependence $R(\lambda)$.

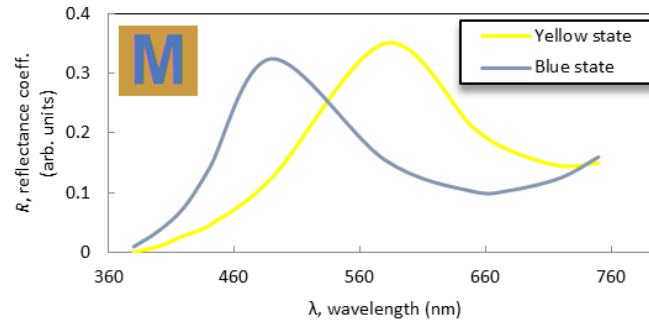


Figure 4. Model predictions. Reflectance spectra of the security film. Inset: computer-simulated image based on the LC parameters of the case study.

The governing parameters of supertwisted nematic (STN) liquid crystals are defined in Table 1. Specification of the boundary conditions enables the director alignment along the z -axis (perpendicular to the substrates) to be calculated. Then, the LC layer is represented as a multi-sublayer model for the application of Jones-matrix formalism.

Table 1. Liquid crystal parameters for the case study.

Twist Angle, Φ	240°
Thickness	5 μm
Elastic constants	$K_{11} = 1.28 \times 10^{-11}$ N, $K_{22} = 7.25 \times 10^{-12}$ N, $K_{33} = 2.06 \times 10^{-11}$ N
Refractive indices parallel and perpendicular to the optical axis	$n_{\parallel} = 1.6$, $n_{\perp} = 1.482$

Plots in Figure 4 summarize the simulation results with the material parameters (Table 1). The computer-generated image in the inset was obtained from the theory of partial coherence, which is relevant for partial reflections at surfaces that have larger distances and can be observed under the given experimental conditions [30]. Static consideration of the problem allows us to note that the values of elastic and dielectric constants do not have critical importance.

The color and contrast ratio are defined by the fast axis of the wave plate and the optical path difference. Successive simulation of the reflected color spectra in MOUSE-LCD results in blue and yellow monochromatic images with a reflectance coefficient greater than 30%. Then, the images were merged into a single letter “M” (see Figure 4).

When the value of Δnd is known, the change of the color coordinates is due to the modification of the polarization. Since the thickness–birefringence product plays a dominant role in Formula (1), then small changes in Δnd result in a considerable shift in the color spectrum. The layer thickness d is adjusted in such a way that the device appears blue at normal light incidence and violet to blue when tilting around the reference axis in the regions, where the optical axis is parallel to the reference axis, while the color in the other regions simultaneously changes from blue to yellow. If the layer is tilted, the information appears yellow on a blue background or vice versa. Other colors can be generated by optimization of the LC layer thickness.

3.2. Field Sequential Color Ferroelectric LCD

An inherent problem of LCDs is the absorption of backlight emissions in the color filters (70%) and polarizers (up to 60%). Fast manipulation of the optical phase delay

together with a modulated backlight allows color filters to be avoided, by using a Field Sequential Color (FSC) system. This approach simultaneously triples the spatial resolution and optical efficiency, but the FSC system requires fast switching and driving transistors, since typical values of turn-on time are about ~ 0.3 ms. This contradiction shows that the peak brightness must be optimized.

Sequential transmission of colors results in an intrinsic effect known as color breakup. In order to avoid this issue, LC response time in the FSC display must be sufficiently small. Previous examination of ferroelectric liquid crystals (FLC) revealed their high potential due to their sub-millisecond response time and properties of photoalignment [31]. Meanwhile, the driving circuits for modulation of grey levels are complicated, but provide an acceptable low-voltage response time. The electrically suppressed helix mode based on FLC fulfills the requirements of an FSC display system (Figure 5a) [32]. The main properties of the ESH mode are the following: (i) shock stability (Figure 5b), (ii) fast response time (24–32 μ s) at the voltage of ± 2 V/ μ m, and (iii) the contrast ratio superiors 10,000:1 (Figure 5d). Note that the display recovers to the acceptable contrast ratio for the human eye just in 8–10 s after the shock impact.

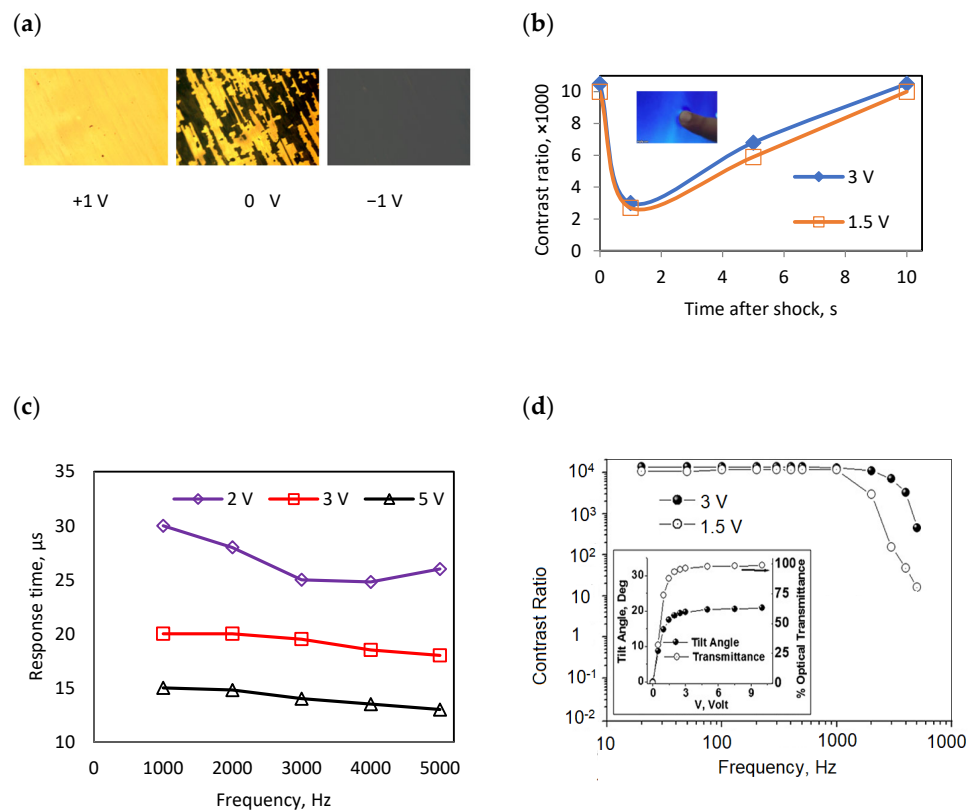


Figure 5. Electrooptical response of ESH FLC mode: (a) optical microphotographs of bright and dark states (± 1 V) [32]; (b) mechanical stability, i.e., full recovery of the optical image after the mechanical shock; (c) frequency dependence of ESH FLC response time for different voltages; (d) contrast ratio of ESH FLC as a function of frequency for $\lambda = 630$ nm [33].

The response time of a reflective FLC cell driven at 5 kHz by an electric field of 5 V constitutes about 14 μ s. Pulse width modulation (PWM) is used to control the switching and provide grey levels. The main advantage of PWM is that the power loss in the switching device remains low.

Further development of photoaligned FSC FLC displays is aimed at the following: (i) fundamental study of electro-optical modes used for switching; (ii) understanding the physical mechanisms of FLC interaction with the photoaligned surface exhibiting a different photosensitive nature to produce stable alignment within a large surface area;

(iii) synthesis of new FLC materials with fast switching and a sufficient number of grey levels (V-shaped switching); (iv) implementation of advanced prototypes of FSC FLC displays; and (v) investigation of operation modes for efficient addressing of FLC displays.

3.3. Liquid Crystal Sensors

Liquid crystal materials are highly sensitive to weak external fields and can work as indicators of a number of parameters. They are sensitive to temperature, concentration, pressure, mechanical stress, electric fields, magnetic fields, pH, environmental pollution, etc. [34–36]. Based on these materials, it is possible to build smart systems based on molecular recognition. Below, we consider several types of sensors for biomedical applications and fiber optics.

3.3.1. LC polarimetry Sensor

The observation of biological processes at the molecular level shows that small molecules, biomarkers, and biological agents play crucial roles. In particular, biomarkers have attracted particular attention in diagnosing diseases and optimizing treatment based on precise measurement of their amounts in body fluids. Studying the methods for early identification of cancer cells is necessary for early diagnosis of cancer and timely selection of treatment methods. Currently, analytical diagnostic techniques are relevant for clinical applications. Examples of such techniques are Raman spectroscopy of tissues [37,38] and surface plasmon resonance effects in biosensors [39]. Liquid crystals have also become an emerging analytical tool [40].

The sensitivity of LCs to translate properties of the bounding surface to an optical signal makes it possible to record chemical and biological changes in biological tissues using polarized light. Multiple light scattering affects the degree of polarization and the Stokes parameters of reflected light. The change in polarized light reflection by a biological object allows one to extract information about the structural state of the sample (tissue, cell, or saliva) and the presence of morphological changes (Figure 6a). These changes can be detected by a simple pattern recognition [41,42].

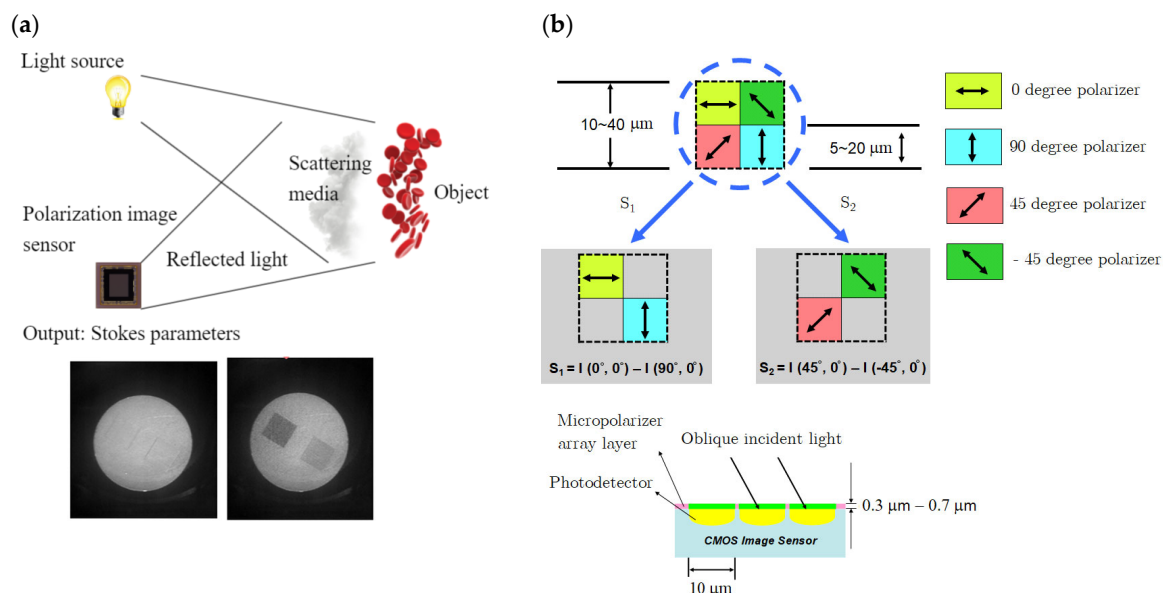


Figure 6. Color online. Polarimetry image sensors for a simultaneous detection of the Stokes parameters of output optical image including “invisible objects” (grayscale transmission/reflection images) with high resolution.

It is possible to manufacture a matrix of micro-polarizers to record the Stokes parameters in combination with multiple microscopic images of a tissue [43]. Theoretical and

experimental study of the matrix can create the prerequisites for rapid analysis of tissues for the detection of pathogens [44].

A polarimetry sensor uses a patterned micro-polarizer array, which is fabricated by photoalignment in combination with a metal-oxide-semiconductor (CMOS) backplane image sensor for the simultaneous detection of four Stokes parameters in an output optical image (Figure 6b) [44]. There is a stringent requirement for normal light incidence, which makes applications with oblique incident light infeasible. The size of the micro-polarizer array pixels is $5 \times 5 \mu\text{m}$, and a thickness of $0.95 \mu\text{m}$ is achieved by using photoalignment of SD1 nanolayer across the 400–700 nm visible spectrum range. The micro-polarizer array includes a multi-domain matrix of polarizers with a patterned SD1 layer, which is used to align another azo dye molecular layer (azo dye 1, AD1), which is capable of polarizing light. The proposed geometry of micro-polarizers makes it possible to detect three Stokes parameters of light (S_0, S_1, S_2). The light transmitted through each domain will have different polarization characteristics ($0^\circ, 90^\circ$, or $\pm 45^\circ$). Right- or left-handed circular polarized light can be detected by using a phase retarder, placed after the micro-polarizer array.

Thus, the sensor includes the formation of a photosensitive surface. The proposed fabrication technology completely removes the need for any selective etching during the fabrication/integration process of the micro-polarizer array. The proposed device is completely compatible with the CMOS backplane and requires only spin-coating followed by ultraviolet exposure.

3.3.2. Fiber/LC Sensor

The linear response in a reflective deformed helix ferroelectric (DHF) FLC cell enables applications in fiber Bragg grating sensors. These sensors have inherent sensitivity to temperature changes, axial strain, and pressure [45], i.e., observable as a shift in the Bragg wavelength in the reflected/transmitted power spectrum. The sensor head consists of an FLC cell, which acts as a variable electric-field-controlled polarizer. Application of an electric field across the cell leads to rotation of the optical axis around the axis parallel to the electric field, which results in a change in the dielectric tensor. This mechanism is the basis of the sensor functionality (see Figure 7a [46]). Alignment of FLC with the submicron helix pitch is obtained by making a 10 nm thick photoaligned layer on the golden electrode prior to injecting LC into the cell. The operating principle of the LC sensor is as follows: an optical fiber is attached by glue to the top glass substrate. The glass substrate has an aperture, which is fitted for a single-mode optical fiber, and a golden coating in front of the fiber tip is patterned to form a grid with a 200 nm period. Consequently, light travels through the following parts of the device: (1) the front golden electrode (–), which represents a nanowire grid (i.e., a linear polarizer); (2) photoaligned layer (light blue); (3) an LC layer; (4) second alignment layer (light blue); and (5) rear golden electrode (+), which plays the role of a broad band mirror for light reflection into the fiber. The reflected light has linear polarization and the LC cell exhibits a continuous hysteresis-free optical phase delay. The reflectivity can be measured by means of the integrated single-mode fiber using unpolarized light ($\lambda = 1.55 \mu\text{m}$). The operating conditions are chosen to maximize the modulation in reflectance and obtain a linear response $R(V)$, see Figure 7b [47,48]. One can note that at zero voltage, the crossed polarizer's reflectance achieves its maximum value for $\beta = 45^\circ$ and vanishes for $\beta = 0$. Fiber Bragg sensors have already been applied to measure flow velocity and pressure in pipelines.

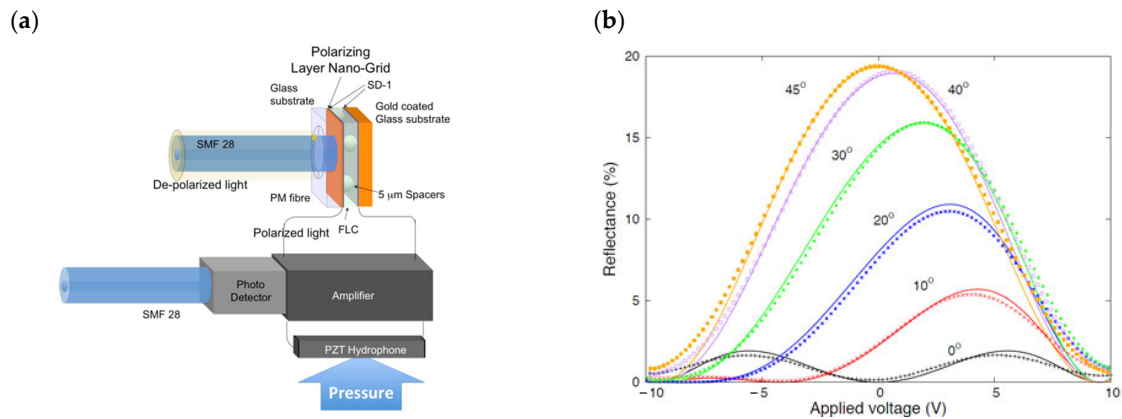


Figure 7. Color online. Fiber/LC-based sensor: (a) Sensor configuration, which includes optical fiber with the Bragg grating in contact with the DHF cell based on SD1 photoalignment (b) and normalized reflectivity measurements (dot lines) and simulations (solid lines) as a function of the static voltage applied to the LC cell for different angles β between the helix axis and the input polarizer.

3.4. Liquid Crystal Lenses

Among LC-based applications, adaptive lenses have been studied for more than 40 years. Pioneering research was carried out in the late 1970s, giving rise to the first proposals of adaptive lenses, known as the works of Berreman et al. [49] and Sato et al. [50]. Originally, the developed adaptive lenses were based on a curved cavity that was filled with LC. A low response time due to high LC layer thickness and inhomogeneity of molecular alignment on curved surfaces represented the main problems of the prototype lens. Due to these issues, this technique was not further developed.

Lenses with electrically tunable focal lengths have a number of potential applications [51]. The absence of moving components in such lenses makes this element base reliable and resistant to mechanical shock. The application of tunable lenses offers a number of interesting results in autofocus cameras, LED light steering applications, and 2D/3D switchable LCDs. Many photonic devices require lenses with a variable focal distance. A zoom lens system usually consists of a group of lenses, with the separation distances between them mechanically adjusted. Mechanical adjusting processes are, as a rule, complicated and bulky. This is the reason for developing a new type of tunable lens that is compact, lightweight, low-cost, and efficient. Such lenses are highly desirable as an element base for adaptive optics, optoelectronics, machine vision, stereo displays, and eyeglasses applications.

Control of the pretilt angle of the director leads to the opportunity for the fabrication of low-power-consuming tunable LC lenses [52]. A laser beam with a Gaussian intensity profile induces a spatially variable pretilt angle ranging between 1 and 89°. In order to generate spatially variable UV irradiance, a mask with a circular structure of radius R is placed at a distance D from the substrate (Figure 8a). Liquid crystal molecules are planar aligned between electrodes. Because the profile of the refractive index $n(x,z)$ depends on the applied electric field, then the corresponding retardation parameter profile $\delta = \pi d \Delta n / \lambda$ also shows smooth parabolic dependences versus the radius of the photomask, where Δn is the effective refractive index between the lens center and its edge (Figure 8b). Investigation of interference patterns shows that the increase in voltage forms declinations in LC cells, and optical properties become distorted (see the inset in Figure 8b) [53].

As was noted in Section 2, the pretilt angle depends on the absorbed energy (see also Figure 2). Therefore, spatially variable UV irradiance can be used to achieve any desired pattern. The light intensity exposed on the substrate was distributed with circular symmetry with the smallest intensity at the center and the largest at the border of the circle. All of these retardation parameter profiles show a parabolic character that is acceptable for all lenses. The possibility of creating optically rewritable lenses has practical implications

in the ophthalmic lens industry as a solution for people whose compensation needs to be changed over time due to age-related physiological changes.

More generally, there exist other photonic elements (e.g., beam steering devices, diffraction gratings, etc.) that can take advantage of photoalignment. However, further research is needed to improve and stabilize the lens profile, which must include the advantages of grayscale masks or control of exposing environments.

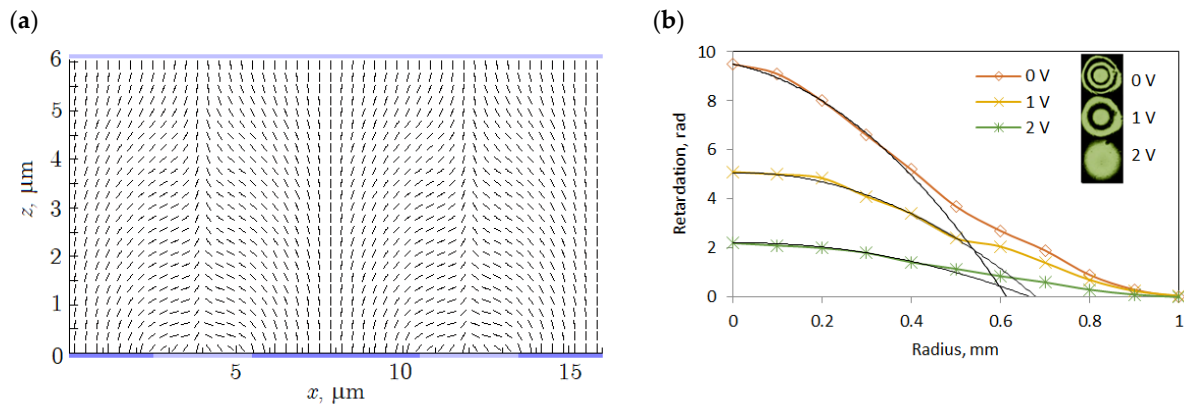


Figure 8. Color online. Liquid crystal lens produced by photoalignment: (a) schematic representation of director distribution in LC lens; (b) retardation parameter profile dependence versus the radius of the circular structure for different voltages, $\Delta n = 0.27$; solid lines represent parabolic approximation. Inset: microphotographs of the spots, produced by LC lens at different applied voltages (spot size: ≈ 0.5 mm, $\lambda = 543$ nm).

3.5. Fresnel Lens

There exist two main traditional methods for the fabrication of Fresnel lenses: electron-beam lithography [54] and thin-film deposition [50]. However, the focusing efficiency and the focal length of the Fresnel lens fabricated in these ways are fixed and the devices are not tunable. This issue is solved by using LCs as optical materials with an electrically modulated refractive index and surface structure by using photoalignment technology.

The desired phase profile is achieved by the electrically controlled effective birefringence of a ferroelectric liquid crystal sandwiched between a flat Fresnel zone electrode substrate and a reference substrate. Fabrication of this lens leads to a flat, thin-film, phase retarder known as the Fresnel lens [55]. The most suitable electro-optic effect for a Fresnel lens is an electrically suppressed helix FLC. Hysteresis-free, sub-millisecond switching time (< 0.1 ms for the voltage of 8 V), absence of a fringe field effect, good electro-optic performance, and shock stability constitute the main properties of electrically suppressed helix FLC [32]. These properties offer numerous possibilities for polarization rotators or shutters for various applications in combination with polarization-dependent passive LC lenses.

The focusing properties of the Fresnel lens are electric-field-controlled, show high diffraction efficiency, and a quick response time. Orthogonal alignment of the domains is achieved by using a hybrid photoalignment technique of LCs (Figure 9a,b), where the dashed lines represent smectic layer normal and θ is the smectic cone angle [56]. Typical radii of the inner domain can range within 250–350 μm . Accordingly, the director can rotate an angle of 2θ in each domain. Orientation of the easy axis between the neighboring zones can make angle β either $\pi/4$ or $\pi/2$ with the switching time of 120 μs and the diffraction efficiency of 37%, which is close to the theoretical limit of 40%. If an FLC Fresnel lens is used with a patterned polarized screen, a projection of a color image becomes possible. Focus (diffractive)/Off (dark) mode occurs when $\beta = \pi/2$ and Focus/Defocus (transmission) mode occurs when $\beta = \pi/4$. A prototype application of the Fresnel lens is depicted in Figure 9c. A focus spot size of 25 μm achieves a diffraction efficiency of 34% for the

diffracted beam of the first order [57]. Note that the light intensity at the focusing spot corresponding to a specific wavelength is governed by the applied voltage and significantly increases illumination at the observation point. Thus, with the described characteristics, photoaligned Fresnel zone plates have significant potential for applications in advanced electro-optical devices.

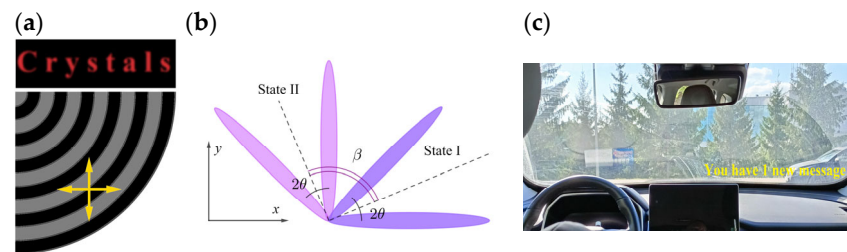


Figure 9. Color online: (a) Schematic representation of the microscopic image of the Fresnel zone plate lens under crossed polarizers (indicated by double arrows) and diffraction profile of the Focus state of an image ($\lambda = 632.8$ nm). (b) Two FLC states correspond to the neighboring Fresnel zones; x -axis corresponds to the direction of the incident polarized light. (c) Image prototype, which can be produced by using a patterned Fresnel zone plate.

4. Conclusions

In this work, we considered the physical mechanisms behind photonic LC devices employing multi-domain photoalignment and phase modulation. We note that photosensitive alignment materials bring new design rules for photonic devices. The main disadvantages of LC phase modulators are dispersion and sensitivity to polarization. The alignment based on a photosensitive azo dye nanolayer can reduce the pixel size since the illumination domain size can be less than 100 nm. The alignment of patterned areas in a single LC cell enables independent optimization of the performance for orthogonal polarizations, whether they need to be identical or different. All these results are promising for the development and fabrication of LC photonic devices with photoinduced structures of long molecular axes. In particular, photoalignment promotes the development of diffractive optical components for augmented-reality displays [58].

We believe that further research in photoaligned multi-domain LC components should concentrate on theoretical developments as well as experimental improvements. Theoretically, photoaligned multi-domain LC systems with wide diffraction angles require a thorough study in addition to the capacity to tailor angular and spectrum response. These issues are important to satisfy the requirements of realistic optical systems. The focus should also be placed on utilizing azo dye nanolayer photoalignment technology to provide experimental demonstrations of multi-domain liquid crystal devices. This is crucial for investigating methods for producing high-resolution polarization holograms, which are capable of utilizing large areas.

Author Contributions: Conceptualization: A.K., V.C. and K.N.; writing—original draft preparation: A.K.; figures and editing: D.C. and A.P. All authors have read and agreed to the published version of the manuscript.

Funding: This research received no external funding.

Data Availability Statement: The original contributions presented in the study are included in the article, further inquiries can be directed to the corresponding author.

Acknowledgments: A.K. acknowledges the financial support of the Ufa University of Science and Technology for the opportunity to visit the Hong Kong University of Science and Technology during the manuscript preparation.

Conflicts of Interest: Author Vladimir Chigrinov was employed by the company Nanjing Jingcui Optical Technology Co., Ltd. The remaining authors declare that the research was conducted in the

absence of any commercial or financial relationships that could be construed as a potential conflict of interest.

References

1. O'Neill, M.; Kelly, S. Photoinduced surface alignment for liquid crystal displays. *J. Phys. D Appl. Phys.* **2000**, *33*, R67. [CrossRef]
2. Ichimura, K. Photoalignment of liquid-crystal systems. *Chem. Rev.* **2000**, *100*, 1847–1874. [CrossRef] [PubMed]
3. Folwill, Y.; Zeitouny, Z.; Lall, J.; Zappe, H. A practical guide to versatile photoalignment of azobenzenes. *Liq. Cryst.* **2021**, *48*, 862–872. [CrossRef]
4. McGinty, C.P.; Kołacz, J.; Spillmann, C.M. Large rewritable liquid crystal pretilt angle by in situ photoalignment of brilliant yellow films. *Appl. Phys. Lett.* **2021**, *119*, 141111. [CrossRef]
5. Iimura, Y.; Saitoh, T.; Kobayashi, S.; Hashimoto, T. Liquid crystal alignment on photopolymer surfaces exposed by linearly polarized UV light. *J. Photopolym. Sci. Technol.* **1995**, *8*, 257–262. [CrossRef]
6. Schadt, M. Liquid crystal displays and novel optical thin films enabled by photo-alignment. *Mol. Cryst. Liq. Cryst. Sci. Technol. Sect. A Mol. Cryst. Liq. Cryst.* **2001**, *364*, 151–169. [CrossRef]
7. Wu, K.-H.; Chen, C.-Q.; Shen, Y.; Cao, Y.; Li, S.-S.; Dierking, I.; Chen, L.-J. Trajectory engineering of directrons in liquid crystals via photoalignment. *Soft Matter* **2023**, *19*, 4483–4490. [CrossRef]
8. Sellers, D. iPhone X (with OLED), iPad Pro (with ProMotion) Win Display Industry Awards. Available online: <https://appleworld.today/iphone-x-with-oled-ipad-pro-with-promotion-win-display-industry-awards/> (accessed on 16 March 2024).
9. Ma, Y.; Zhao, Z.; Morris, S.M.; He, C. Twisted microdomains in liquid crystals for polarization-insensitive phase modulation. *Light Sci. Appl.* **2024**, *13*, 8. [CrossRef] [PubMed]
10. Cheng, Y.-C.; Yuan, Z.-N.; Sun, Z.-B.; Srivastava, A.K. 3-3: Large-FoV Fast LiDAR System based on Electrically Suppressed Helix Ferroelectric Liquid Crystal. *SID Symp. Dig. Tech. Pap.* **2023**, *54*, 9–12. [CrossRef]
11. Srivastava, A.K. LiDAR/3D depth mapping systems using advanced swift FLC photonics (Conference Presentation). In Proceedings of the Emerging Liquid Crystal Technologies XVIII, San Francisco, CA, USA, 1–2 February 2023; p. 1244206.
12. Yoshida, H.; Abe, Y.; Igeta, K.; Higuchi, A.; Kobashi, J.; Tomioka, Y.; Oka, S. Transversely graded polarization volume gratings fabricated by freeform holographic photoalignment. *Opt. Lett.* **2024**, *49*, 121–124. [CrossRef]
13. Chen, F.; Zheng, J.; Xing, C.; Sang, J.; Shen, T. Applications of liquid crystal planer optical elements based on photoalignment technology in display and photonic devices. *Displays* **2024**, *82*, 102632. [CrossRef]
14. Berteloot, B.; Nys, I.; Liu, S.; Neyts, K. Two-Dimensional Liquid-Crystal Photoalignment by Multiple Illumination Steps. *ACS Appl. Opt. Mater.* **2023**. [CrossRef]
15. Chigrinov, V.; Kozenkov, V.; Kwok, H. *Photoaligning: Physics and Applications in Liquid Crystal Devices*; Wiley VCH: Weinheim, Germany, 2008.
16. Chigrinov, V.; Pikin, S.; Verevochnikov, A.; Kozenkov, V.; Khazimullin, M.; Ho, J.; Huang, D.D.; Kwok, H.-S. Diffusion model of photoaligning in azo-dye layers. *Phys. Rev. E* **2004**, *69*, 061713. [CrossRef] [PubMed]
17. Lagerwall, S.T.; Muravski, A.A.; Yakovenko, S.Y.; Konovalov, V.A.; Minko, A.A.; Tsarev, V.P. Pressure-insensitive liquid crystal cell. U.S. Patent US6184967B1, 6 February 2001.
18. Chen, J.; Xu, T.; Zhao, W.; Ma, L.-L.; Chen, D.; Lu, Y.-Q. Photoresponsive thin films of well-synthesized azobenzene side-chain liquid crystalline polynorbornenes as command surface for patterned graphic writing. *Polymer* **2021**, *218*, 123492. [CrossRef]
19. Fang, Q.; Lv, Y.; Yan, Z.; Sun, X.; Shen, J.; Liu, M.; Wang, T.; Chen, J.; Yin, S. Photoalignment of sub-micrometer periodic liquid crystal polarization grating by using the optical imprinting method. *Opt. Express* **2023**, *31*, 13428–13435. [CrossRef] [PubMed]
20. Lim, K.T.; Liu, H.; Liu, Y.; Yang, J.K. Holographic colour prints for enhanced optical security by combined phase and amplitude control. *Nat. Commun.* **2019**, *10*, 25. [CrossRef] [PubMed]
21. Kim, I.; Jang, J.; Kim, G.; Lee, J.; Badloe, T.; Mun, J.; Rho, J. Pixelated bifunctional metasurface-driven dynamic vectorial holographic color prints for photonic security platform. *Nat. Commun.* **2021**, *12*, 3614. [CrossRef] [PubMed]
22. Chen, J.; Yu, F.; Liu, X.; Bao, Y.; Chen, R.; Zhao, Z.; Wang, J.; Wang, X.; Liu, W.; Shi, Y. Polychromatic full-polarization control in mid-infrared light. *Light Sci. Appl.* **2023**, *12*, 105. [CrossRef] [PubMed]
23. Phillip, R.W.; Bleikolm, A.F. Optical coatings for document security. *Appl. Opt.* **1996**, *35*, 5529–5534. [CrossRef]
24. Chen, N.; Chen, L.; Li, Y.; Li, W.; Zhao, Y.; Wang, Z.; Wang, X.; Bu, Y. Design and fabrication of metameric interference thin films based on metal-dielectric structure for optical security devices. *Surf. Coat. Technol.* **2019**, *364*, 392–397. [CrossRef]
25. Schadt, M.; Seiberle, H. Optical Element. U.S. Patent US9643445B2, 9 May 2017.
26. Fan, F. Optical Security Film. Available online: <https://www.youtube.com/watch?v=4L32m74e7HE> (accessed on 15 April 2024).
27. Chigrinov, V.; Kudreyko, A.; Sun, J. Photosensitive Alignment: Advanced Electronic Paper-Based Devices. *Crystals* **2022**, *12*, 364. [CrossRef]
28. Goldstein, D.H. *Polarized Light*; CRC Press: Boca Raton, FL, USA, 2017.
29. Chen, J.; Yu, F.-H.; Huang, H.-C.H.H.-C.; Kwok, H.S.K.H.S. Reflective supertwisted nematic liquid crystal displays. *Jpn. J. Appl. Phys.* **1998**, *37*, 217. [CrossRef]
30. Khoo, I.-C. *Liquid Crystals*; John Wiley & Sons: Hoboken, NJ, USA, 2007; Volume 64.
31. Wyatt, P.; Bailey, J.; Nagaraj, M.; Jones, J. A self-healing ferroelectric liquid crystal electro-optic shutter based on vertical surface-relief grating alignment. *Nat. Commun.* **2021**, *12*, 4717. [CrossRef] [PubMed]

32. Srivastava, A.K.; Chigrinov, V.G.; Kwok, H.S. Electrically suppressed helix ferroelectric liquid crystals for modern displays. *J. Soc. Inf. Disp.* **2015**, *23*, 176–181. [[CrossRef](#)]
33. Guo, Q.; Yan, K.; Chigrinov, V.; Zhao, H.; Tribelsky, M. Ferroelectric liquid crystals: Physics and applications. *Crystals* **2019**, *9*, 470. [[CrossRef](#)]
34. Wang, Y.; Zhao, L.; Xu, A.; Wang, L.; Zhang, L.; Liu, S.; Liu, Y.; Li, H. Detecting enzymatic reactions in penicillinase via liquid crystal microdroplet-based pH sensor. *Sens. Actuators B Chem.* **2018**, *258*, 1090–1098. [[CrossRef](#)]
35. Amin, N.u.; Siddiqi, H.M.; Kun Lin, Y.; Hussain, Z.; Majeed, N. Bovine serum albumin protein-based liquid crystal biosensors for optical detection of toxic heavy metals in water. *Sensors* **2020**, *20*, 298. [[CrossRef](#)] [[PubMed](#)]
36. Balenko, N.; Shibaev, V.; Bobrovsky, A. Mechanosensitive polymer-dispersed cholesteric liquid crystal composites based on various polymer matrices. *Polymer* **2023**, *281*, 126119. [[CrossRef](#)]
37. Mahadevan-Jansen, A.; Richards-Kortum, R.R. Raman spectroscopy for the detection of cancers and precancers. *J. Biomed. Opt.* **1996**, *1*, 31–70. [[CrossRef](#)]
38. Kothari, R.; Jones, V.; Mena, D.; Bermúdez Reyes, V.; Shon, Y.; Smith, J.P.; Schmolze, D.; Cha, P.D.; Lai, L.; Fong, Y. Raman spectroscopy and artificial intelligence to predict the Bayesian probability of breast cancer. *Sci. Rep.* **2021**, *11*, 6482. [[CrossRef](#)]
39. Azzouz, A.; Hejji, L.; Kim, K.-H.; Kukkar, D.; Souhail, B.; Bhardwaj, N.; Brown, R.J.; Zhang, W. Advances in surface plasmon resonance-based biosensor technologies for cancer biomarker detection. *Biosens. Bioelectron.* **2022**, *197*, 113767. [[CrossRef](#)] [[PubMed](#)]
40. Pourasl, M.H.; Vahedi, A.; Tajalli, H.; Khalilzadeh, B.; Bayat, F. Liquid crystal-assisted optical biosensor for early-stage diagnosis of mammary glands using HER-2. *Sci. Rep.* **2023**, *13*, 6847. [[CrossRef](#)] [[PubMed](#)]
41. Wang, Z.; Xu, T.; Noel, A.; Chen, Y.-C.; Liu, T. Applications of liquid crystals in biosensing. *Soft Matter* **2021**, *17*, 4675–4702. [[CrossRef](#)] [[PubMed](#)]
42. Rajesh; Gangwar, L.K.; Mishra, S.K.; Choudhary, A.; Biradar, A.M.; Sumana, G. Technological advancements in bio-recognition using liquid crystals: Techniques, applications, and performance. *Luminescence* **2023**, *38*, 811–833. [[CrossRef](#)] [[PubMed](#)]
43. Hsu, W.-L.; Myhre, G.; Balakrishnan, K.; Brock, N.; Ibn-Elhaj, M.; Pau, S. Full-Stokes imaging polarimeter using an array of elliptical polarizer. *Opt. Express* **2014**, *22*, 3063–3074. [[CrossRef](#)] [[PubMed](#)]
44. Zhao, X.; Bermak, A.; Boussaid, F.; Du, T.; Chigrinov, V.G. High-resolution photoaligned liquid-crystal micropolarizer array for polarization imaging in visible spectrum. *Opt. Lett.* **2009**, *34*, 3619–3621. [[CrossRef](#)]
45. Crawford, G.P. Electrically switchable Bragg gratings. *Opt. Photonics News* **2003**, *14*, 54–59. [[CrossRef](#)]
46. Brodzeli, Z.; Silvestri, L.; Michie, A.; Guo, Q.; Pozhidaev, E.P.; Chigrinov, V.; Ladouceur, F. Sensors at your fibre tips: A novel liquid crystal-based photonic transducer for sensing systems. *J. Light. Technol.* **2013**, *31*, 2940–2946. [[CrossRef](#)]
47. Kiselev, A.D.; Pozhidaev, E.P.; Chigrinov, V.G.; Kwok, H.-S. Polarization-gratings approach to deformed-helix ferroelectric liquid crystals with subwavelength pitch. *Phys. Rev. E* **2011**, *83*, 031703. [[CrossRef](#)]
48. Brodzeli, Z.; Silvestri, L.; Michie, A.; Guo, Q.; Pozhidaev, E.P.; Chigrinov, V.; Ladouceur, F. Reflective mode of deformed-helix ferroelectric liquid crystal cells for sensing applications. *Liq. Cryst.* **2013**, *40*, 1427–1435. [[CrossRef](#)]
49. Berreman, D.W. Variable focus liquid crystal lens system. U.S. Patent US4190330A, 26 February 1980.
50. Sato, S. Liquid-crystal lens-cells with variable focal length. *Jpn. J. Appl. Phys.* **1979**, *18*, 1679. [[CrossRef](#)]
51. Lin, Y.-H.; Cheng, W.-C.; Reshetnyak, V.; Huang, H.-H.; Huang, T.-W.; Cheng, C.-C.; Wu, Y.-H.; Yang, C.-L. Electrically tunable gradient-index lenses via liquid crystals: Beyond the power law. *Opt. Express* **2023**, *31*, 37843–37860. [[CrossRef](#)]
52. Algorri, J.F.; Zografopoulos, D.C.; Urruchi, V.; Sánchez-Pena, J.M. Recent advances in adaptive liquid crystal lenses. *Crystals* **2019**, *9*, 272. [[CrossRef](#)]
53. Fan, F.; Srivastava, A.K.; Du, T.; Tseng, M.C.; Chigrinov, V.; Kwok, H.S. Low voltage tunable liquid crystal lens. *Opt. Lett.* **2013**, *38*, 4116–4119. [[CrossRef](#)] [[PubMed](#)]
54. Sato, S.; Sugiyama, A.; Sato, R. Variable-focus liquid-crystal Fresnel lens. *Jpn. J. Appl. Phys.* **1985**, *24*, L626. [[CrossRef](#)]
55. Mukherjee, S.; Yuan, Z.-N.; Sun, Z.-B.; Li, A.-R.; Kang, C.-B.; Kwok, H.-S.; Srivastava, A.K. Fast refocusing lens based on ferroelectric liquid crystals. *Opt. Express* **2021**, *29*, 8258–8267. [[CrossRef](#)]
56. Chigrinov, V.G.; Srivastava, A. Ferroelectric liquid crystal cells for advanced applications in displays and photonics. *Mol. Cryst. Liq. Cryst.* **2014**, *595*, 39–49. [[CrossRef](#)]
57. Tsukamoto, Y.; Ozaki, M. Liquid crystal micro-Fresnel zone plate with fine variable focusing properties. *Opt. Contin.* **2023**, *2*, 1889–1900. [[CrossRef](#)]
58. Zou, J.; Li, L.; Wu, S.-T. Gaze-matched pupil steering Maxwellian-view augmented reality display with large angle diffractive liquid crystal lenses. *Adv. Photonics Res.* **2022**, *3*, 2100362. [[CrossRef](#)]

Disclaimer/Publisher’s Note: The statements, opinions and data contained in all publications are solely those of the individual author(s) and contributor(s) and not of MDPI and/or the editor(s). MDPI and/or the editor(s) disclaim responsibility for any injury to people or property resulting from any ideas, methods, instructions or products referred to in the content.